High-performance photocatalytic and piezoelectric properties of two-dimensional transition metal oxyhalide $ZrOX_2$ (X = Br, I) and their Janus structures

Qiu Yang,[1] Dan Wang,[1] Zhao-Yi Zeng,[2,*] Hua-Yun Geng,[3] and Xiang-Rong Chen[1,†]
[1]*College of Physics, Institute of Atomic and Molecular Physics, Sichuan University, Chengdu 610065, China*
[2]*College of Physics and Electronic Engineering, Chongqing Normal University, Chongqing 401331, China*
[3]*National Key Laboratory for Shock Wave and Detonation Physics Research, Institute of Fluid Physics, CAEP, Mianyang 621900, China*

(Received 3 September 2023; revised 3 December 2023; accepted 13 December 2023; published 11 January 2024)

As an emerging type of two-dimensional (2D) family, transition metal oxyhalides with the chemical formula MOX_2 have been studied in recent years. Inspired by the successful synthesis of $ZrOI_2$ monolayer with excellent photocatalytic and piezoelectric properties, we conducted a systematic and comprehensive investigation of $ZrOX_2$ (X = Br, I) and its Janus ZrOBrI monolayers using first-principles calculations. The results show that the mechanically, dynamically, and thermally stable $ZrOX_2$ and Janus ZrOBrI are indirect-gap semiconductors with band gaps ranging from 1.89 to 3.48 eV by the hybrid density functional HSE06 method. Besides, their valence-band minimum and conduction-band minimum can straddle the redox potential of water at pH = 0, respectively. Interestingly, due to the optimal band alignment mechanism, the band-edge position of Janus ZrOBrI with an intrinsic electric field does not expand. Moreover, biaxial compressive strain (within −6%) effects on the band alignments and band gaps are discussed. What is more, strong anisotropy and high optical absorption in the visible-ultraviolet region ($\sim 10^5\ \mathrm{cm}^{-1}$) render these monolayers fantastic polarizers and photoelectronic devices. Besides, the orientation-dependent carrier mobility of these monolayers is much higher than that of many other 2D semiconductors, making them potential electronic and photocatalytic devices. For piezoelectric performance, all of these monolayers exhibit a considerable in-plane transverse piezoelectric coefficient d_{21}, reaching about 20 pm/V. Furthermore, the Janus ZrOBrI possesses additional out-of-plane piezoelectric responses due to structural mirror asymmetry. Under AC stacking mode, multilayer Janus ZrOBrI has appreciable vertical piezoelectric coefficients d_{31} and d_{32}, reaching 1.17 and 4.61 pm/V, respectively. Our findings highlight that all three monolayers are multifunctional devices, especially in the fields of photocatalysis and piezoelectricity.

DOI: 10.1103/PhysRevB.109.035411

I. INTRODUCTION

With the continuous depletion of fossil fuels and the increasing severity of environmental pollution, it is urgent to find clean, efficient, and environmentally friendly renewable energy sources. Hydrogen production based on photocatalytic water splitting is considered to be one of the most suitable technologies for this purpose [1]. Commonly, a high-performance photocatalyst for water splitting should possess these key characteristics, e.g., an appropriate band gap larger than 1.23 eV, a suitable band-edge energy position to straddle the redox potential of water ($E_{H^+/H_2} = -4.44$ eV, $E_{O_2/H_2O} = -5.67$ eV) [2], and high carrier mobility to enhance the transport efficiency of photogenerated holes and electrons at the water interface [3], as well as the strong absorption of visible light to effectively harvest solar energy [4].

Since the successful fabricating of graphene in 2004 [5], two-dimensional (2D) materials have been extensively studied due to their remarkable physical and chemical properties [6–9]. Compared to three-dimensional (3D) materials, high carrier mobility, excellent optical absorption, strain-tunable band gaps, and admirable specific surface areas render 2D materials promising candidates for photocatalysts [10–15], such as graphitic carbon nitride (g−C_3N_4) [16], MXenes [17], and transition metal chalcogenides (TMDs) [18,19]. Particularly, 2D Janus materials with an intrinsic electronic field (EF) will not only relieve the restriction of band-gap requirement but also accelerate the separation of carriers to different surfaces [20]. Inspired by the successful synthesis of the Janus MoSSe monolayer in 2017 [21], Ma *et al.* [15] explored the potential application of the Janus MoSSe monolayer as a wide solar-spectrum water-splitting photocatalyst. Besides, the photocatalytic ability of other new types of Janus has also been widely investigated recently, such as Janus M_2XY (M = Ga, In; X/Y = S, Se, Te) [22], Janus PdPSeX (X = O, S, Se) [23], Janus $WSSiN_2$ [24], and Janus $XMInZ_2$ (X = Cl, Br, I; M = Mg, Ca; Z = S, Se, Te) [25].

Alongside photocatalytic water splitting to produce hydrogen, piezoelectricity is another major energy conversion technology that harvests electricity from mechanical motion [26,27]. Myriads of 2D materials have been reported as potential piezoelectric devices, such as TMDs [28,29], hexagonal boron nitride [30], and graphene nitride [31]. Generally, the piezoelectric polarization of traditional 2D compounds is confined to the basal plane, which prevents their flexibility of piezoelectric device operations in the vertical direction.

*zhaoyizeng@cqnu.edu.cn
†xrchen@scu.edu.cn

Fortunately, 2D Janus materials will break this restriction, and display outstanding both in-plane and out-of-plane piezoelectricity due to the mirror asymmetry in the z axis. Dong *et al.* [32] reported that the synthesized Janus *MXY* (M = Mo, W; X/Y = S, Se, Te) held both strong in-plane and weak out-of-plane piezoelectric polarizations when an in-plane uniaxial strain was applied in monolayers. For multilayer MoSTe, the piezoelectric coefficient d_{33} can reach 5.7–13.5 pm/V, greater than that of the state-of-the-art 3D piezoelectric materials such as AlN ($d_{33} = 5.1$ pm/V) and GaN ($d_{33} = 3.1$ pm/V) [33]. Additionally, novel types of Janus with considerable in-plane and out-of-plane piezoelectric coefficients have been predicted to be prevalent piezoelectric materials [34,35].

Until now, 2D traditional materials with both excellent photocatalytic and unique piezoelectric properties remain scarce, so it is necessary to explore new 2D materials and their Janus forms to find multifunctional devices capable of generating hydrogen and converting energy [36]. As an emerging type of 2D family, transition metal oxyhalides with the chemical formula MOX_2 have been reported recently [37–39]. Particularly, Alam *et al.* [40] showed that ferroelectric $TiOX_2$ and multiferroelectric VOX_2 (X = F, Cl, Br) monolayers have excellent in-plane piezoelectric responses, ranging from 29.03 to 37.76 pm/V. Based on first-principles calculations, Song *et al.* [41] found that monolayer $TiOCl_2$ is expected to be used in solar cells and other optoelectronic devices as an efficient light-absorbing material. In the latest experimental success, 2D $NbOI_2$ with anisotropic electronic and optical properties has been fabricated [42]. Subsequently, Wu *et al.* discovered the high piezoelectric performance of layered $NbOI_2$ [43]. In addition, Pan *et al.* [44] pointed out that anisotropic $NbOX_2$ (X = Cl, Br, I) monolayers are potential candidates for photocatalytic water splitting with high solar-to-hydrogen efficiency at different conditions. More interestingly, Su *et al.* [45]. predicted that Janus NbO*XY* (X, Y = Cl, Br, I; $X \neq Y$) monolayers can be versatile semiconductors, which can be used in flexible electronics, optoelectronic, UV photonics, piezoelectric, and photocatalytic applications.

Triggered by these above, in this work we focused on the $ZrOX_2$ (X = Br, I) monolayers and their corresponding Janus structures, comprehensively and systematically investigated the electronic, optical, piezoelectric, and photocatalytic water-splitting properties of $ZrOX_2$ (X = Br, I) and their Janus monolayer. Our results show that the pristine $ZrOX_2$ monolayers are dynamically, thermally, and mechanically stable, while for Janus Zr*OXY* monolayers, except for Janus ZrOBrI, the other two Janus monolayers (ZrOBrCl, and ZrOClI) have imaginary frequency in phonon spectra. Furthermore, $ZrOBr_2$, $ZrOI_2$, and Janus ZrOBrI monolayers are found to be semiconductors with indirect band gaps of 3.48, 1.89, and 2.10 eV, respectively. All these monolayers have suitable band-edge positions for the overall water splitting in acidic conditions, and the effect of biaxial compressive strain (within −6%) is also considered. Additionally, pristine $ZrOX_2$ and Janus ZrOBrI monolayers present excellent light absorption and anisotropic high-carrier mobility. Moreover, unlike other common 2D piezoelectric materials, these three monolayers have large in-plane transverse piezoelectric responses, reaching about 20 pm/V. Under the AC stacking, multilayer Janus ZrOBrI has an appreciable vertical piezoelectric coefficient d_{32}, reaching 4.61 pm/V. These results reveal that these monolayers can be promising photocatalysts and energy-conversion devices.

II. COMPUTATIONAL DETAILS

All the calculations were performed using the Vienna *ab initio* Simulation Package (VASP) based on density-functional theory (DFT) [46–49]. The projected augmented wave was adopted for the ion-electron interactions, where generalized gradient approximation (GGA) in the scheme of Perdew-Burke-Ernzerhof (PBE) was used to describe the exchange-correlation functions of electrons [50–53]. A kinetic energy cutoff of 600 eV and a Gamma scheme $17 \times 16 \times 1$ k point were selected during the geometry optimization and self-consistent calculations. The convergence criteria of force and energy difference were set to 1×10^{-4} eV/Å and 1×10^{-8} eV, respectively. To prevent interlayered interactions, a vacuum layer of 30 Å was considered along the z direction, and the DFT-D3 method of Grimme was adopted to delineate the potential van der Waals interactions [54,55]. A dipole correction in the normal direction was included throughout the Janus ZrOBrI calculations [56]. Based on the finite-displacement method at the PBE level, a greater than $4 \times 4 \times 1$ supercell with $4 \times 3 \times 1$ k point was constructed to obtain phonon dispersions using the PHONOPY code [57]. To evaluate the thermal stability of these monolayers, a $4 \times 4 \times 1$ supercell was expanded to perform the *ab initio* molecular dynamics (AIMD) simulations in the canonical (*NVT*) ensemble at 300 K for 8 ps with a time step of 2 fs. To appraise the mechanical stability, the finite-difference method was adopted to attain the elastic coefficients.

As it is well known that DFT-GGA calculations underestimate band gaps of semiconductors, the hybrid density functional (HSE06) [58,59] and single-shot *GW* (G_0W_0) [60–62] methods were adopted. In the G_0W_0 calculations, the quasiparticle energies were obtained from the DFT-GGA wave functions. A k point set to $15 \times 15 \times 1$ and a cutoff energy of 400 eV were used, and the number of bands was increased to 128. Then, we used the maximally localized Wannier function as implemented in the WANNIER90 package [63] to interpolate the quasiparticle band structure, where p orbitals of halogen atoms and the s- and d orbitals of Zr atoms were chosen for the initial projections. Because of the heavy element I, the spin-orbital coupling (SOC) [64] effect was also considered at the HSE06 level. To measure the optical response and corresponding exciton binding energies of these systems, the Bethe-Salpeter equation (BSE) [65] calculations were carried out on top of the single-shot G_0W_0 within the Tamm-Dancoff approximation. The eight highest valence bands and the eight lowest conduction bands are included as the basis for excitonic eigenstates. To quantify the carrier mobility, the deformation potential (DP) theory [66,67] and Boltzmann theory were implemented at the PBE level. A constant scattering time (τ = 10fs) and a denser k-point sampling (2 times denser than that used in the geometry optimization) were set when solving the Boltzmann transport equation (BTE). In the BTE method, the effective mass was calculated by BOLTZTRAP code [68] and extracted by PYMATGEN code [69], respectively, and the carrier mobility was obtained by

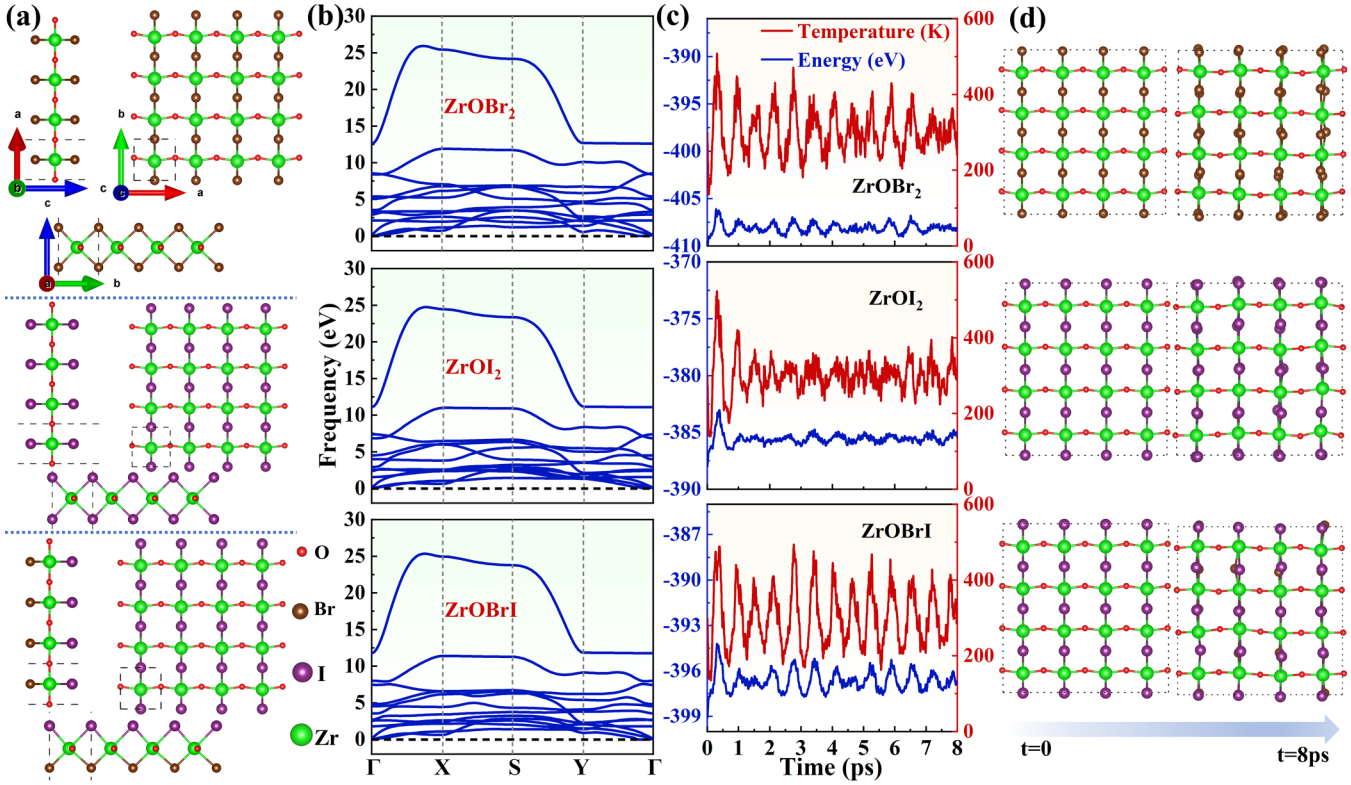

FIG. 1. (a) The optimized crystal structures of ZrOX_2 (X = Br, I) and Janus ZrOBrI monolayers, where the black dashed lines represent the unit cell. (b) Phonon spectra and (c) AIMD simulations at 300 K for ZrOX_2 and Janus ZrOBrI monolayers, where the blue lines and the red lines represent the variation of the total energy and temperature with time, respectively. (d) The original (left) and final (right) crystal structures after AIMD simulations with 8 ps. The blacked dashed lines represent the supercell by 4 × 4 × 1.

the formula: $\mu = \frac{\sigma}{ne}$, where σ and n are, respectively, conductivity and carrier concentration computed by the BOLTZTRAP code. Within the density-functional perturbation theory [70], piezoelectric stress coefficients can be given directly from the VASP code. Due to the 3D periodic boundary conditions, the 2D elastic coefficients and piezoelectric stress coefficients should be corrected by the length of the unit cell in the z direction: $C_{ij}^{2D} = zC_{ij}^{3D}$ and $e_{ij}^{2D} = ze_{ij}^{3D}$ [71].

III. RESULTS AND DISCUSSION

A. Structural stabilities

The optimized geometric structures of ZrOX_2 (X = Br, I) and Janus ZrOBrI monolayers are shown in Fig. 1(a), and have an orthorhombic form with space group *Pmm*2 (No. 25) for ZrOX_2 and *Pm* (No. 6) for Janus ZrOBrI. The Janus nature of ZrOBrI originated from the two outer sublayers of nonequivalent halogen atoms sandwiching the central Zr atom. The rectangular lattice exhibited as strongly anisotropic because of different compositions along the x (O-Zr-O) and y (X-Zr-X) directions. The optimized structural parameters of these specific monolayers are summarized in Table I, and the obtained results accord well with the previous research [72]. Notably, the Zr cation spontaneously displaced away from the structural center, giving rise to the long and short Zr–X bonds along the y direction, whereas Zr–O bonds are the same. Furthermore, the larger the radius of the halogen atom, the greater the lattice constants and bond lengths. The relevant parameters of Janus ZrOBrI monolayer lie between the values of non-Janus ZrOBr$_2$ and ZrOI$_2$ monolayers.

Based on these reliable optimized structures, we next examined the (i) dynamical stability; (ii) thermal stability; (iii) mechanical stability; and (iv) experimental feasibility of these monolayers. As shown in Fig. 1(b), being nearly free of soft phonon modes in the phonon spectra indicated these three monolayers were dynamically stable. Since each unit cell contained 4 atoms, there were 12 phonon modes that could be observed throughout the Brillouin zone (BZ), which were composed of three acoustic modes and nine optical modes. It is noteworthy that the phonon spectra of Janus ZrOBrCl and Janus ZrOClI were also calculated, as shown in Fig. S1 in the Supplemental Material [73]. However, these results showed that both Janus ZrOBrCl and Janus ZrOClI monolayers are not dynamically stable due to the large imaginary frequency, and thus we will only consider Janus ZrOBrI monolayer in subsequent calculations. Additionally, the AIMD simulations of investigated monolayers revealed slight energy fluctuations during 8 ps at 300 K, with tiny structure distortion and no broken bonds, thus verifying the thermal stability of ZrOX_2 and Janus ZrOBrI monolayers at room temperature [shown in Figs. 1(c)–1(d)]. To examine mechanical stability, the independent elastic constants of these monolayers were computed, and the result showed that all these compounds indeed met the Born criteria [74], namely, $C_{11}C_{22} - C_{12}^2 > 0$ and $C_{66} > 0$ (seen in Table IV).

TABLE I. The calculated lattice constants (a and b) (Å), monolayer thickness h (Å), bond lengths (d_{Zr-X1}, d_{Zr-X2}, d_{Zr-O}) (Å), cohesive energy E_{coh} (eV/atom), band gaps from HSE (E_g^{HSE}), HSE+SOC ($E_g^{HSE+SOC}$), and G_0W_0 ($E_g^{G_0W_0}$) (eV) levels of $ZrOX_2$ and Janus ZrOBrI.

Materials	a	b	h	d_{Zr-X1}	d_{Zr-X2}	d_{Zr-O}	E_{coh}	E_g^{HSE}	$E_g^{HSE+SOC}$	$E_g^{G_0W_0}$
$ZrOBr_2$	3.89(3.88[a])	3.89(3.88[a])	3.87	2.65	2.85	1.97	5.35	3.48(3.47[a])	3.44	4.98
$ZrOI_2$	3.95(3.94[a])	4.10(4.11[a])	4.24	2.88	3.03	1.99	4.94	1.89(1.83[a])	1.84	3.34
ZrOBrI	3.93	4.00	4.04	2.66(2.87)	2.82(3.03)	1.98	5.14	2.10	2.07	3.62

[a]Obtained by Yang *et al.* from DFT calculations [72].

To assess the thermodynamic stability and experimental synthesizability of these monolayers, we figured out the cohesive energy by the following formula:

$$E_{coh} = \frac{N_{Zr}E_{Zr} + N_{Br}E_{Br} + N_I E_I + N_O E_O - E_{ML}}{N_{tot}}, \quad (1)$$

where N_{Zr}, N_{Br}, N_I, and N_O are the numbers of Zr, Br, I, and O atoms per unit cell, respectively. N_{tot} is the total number of atoms in the specialized monolayer. E_{Zr}, E_{Br}, E_I, E_O, and E_{ML}, respectively, refer to the energies of isolated Zr, Br, I, and O atoms, and the total static energy of the composed specific monolayer. The computed results are given in Table I.

It is known that the positive E_{coh} indicates binding, and the larger the value, the more stable the structure. In Table I, for considered monolayers, the calculated values of the cohesive energy within the range of 4.94 to 5.35 eV/atom are similar to those of already synthesized phosphorene (3.48 eV/atom) [75] and MoS_2 (5.02 eV/atom) [76], implying the promising feasibilities of these compounds in the future experiment.

B. Electronic structures

The projected band structures and projected density of states of $ZrOX_2$ and ZrOBrI monolayers computed via the HSE06 method are shown in Fig. 2(a). It can be observed that the $ZrOBr_2$, $ZrOI_2$, and ZrOBrI monolayers are semiconducting with indirect band gaps (3.48, 1.89, and 2.10 eV, respectively), and their valence-band maxima (VBMs) locate at the Y point, while the conduction-band minima (CBMs) reside at the Γ point. The band gaps of other transition metal oxyhalides MOX_2 and their Janus monolayers MOXY were listed in Table S1 in the Supplemental Material [73] for comparison. From the projected electronic bands, we can see that the main contributors to the valence-band regions are the p states of halogen atoms, whereas the conduction-band regions dominantly originate from Zr-4d states. Specifically, all CBMs are predominantly composed of the Zr-d_{z^2} states, and VBMs mainly comprise the Br-p_x, and I-p_x states for $ZrOBr_2$, and $ZrOI_2$ monolayers, respectively. Because of the electronegativity, the Br-p states have lower energy than I-p; then, the VBM of Janus ZrOBrI monolayer mainly comes from the I-p_x. Additionally, due to the presence of heavy element I, the SOC effect at the HSE06 level was also considered. As shown in Fig. S2 in the Supplemental Material [73], the SOC correction affects the band structures of these monolayers slightly; thus, we did not take it into account in the forthcoming electronic properties calculations. What is more, band structures and gaps calculated by the G_0W_0 method are also shown in Fig. S3 (see the Supplemental Material [73]) and Table I for comparison. Obviously, band structures are similar in the two different methods, but band-gap values obtained by G_0W_0 are significantly greater than those from HSE06 due to the consideration of electron-electron interactions.

To get the charge-transfer information, the electron localization function and Bader charge of the pristine $ZrOX_2$ and Janus ZrOBrI monolayers were analyzed. The charge depletion around Zr atoms, and charge localization around O and halogen atoms, as shown in Fig. S4 in the Supplemental Material [73], means that Zr atoms lose electrons while O and halogen atoms gain electrons. For the $ZrOBr_2$ structure, we found that 1.196 e transfers from the Zr to O atoms, and 0.568 e transfers from the Zr to Br atoms. Besides, for the $ZrOI_2$ structure, 1.204 e transports from the Zr to O atoms, and 0.502 e transports from the Zr to I atoms. These are in line with the electronegativity difference: O (3.44) > Br (2.96) > I (2.66) > Zr (1.33). In the Janus ZrOBrI monolayer, about 53% of the total transferred charge is delivered to the O atoms, and the rest is sent to the halogen atoms (0.572 e to the Br atoms, 0.499 e to the I atoms). The Br atoms receive more charge compared to the I atoms because of the large electronegativity in Br atoms. Such difference will result in a potential gradient perpendicular to the basal plane, forming an intrinsic electric field between the upper and lower layers.

Finally, the band-decomposed charge densities of VBM and CBM were plotted to visualize the spatial distribution of carriers. As shown in Fig. 2(c), the CBMs and VBMs of pristine $ZrOX_2$ are uniformly distributed around the upper and lower sides, while for Janus ZrOBrI, the VBM mainly distributes at the I side and the CBM mainly distributes at the Zr and Br side. The spatial separation of photogenerated electrons and holes can reduce the possibility of carrier recombination, which is advantageous for photocatalytic water splitting. Figure 2(b) exhibits the planar-average electrostatic potentials along the z axis. Consistent with the Bader charge analysis, different from the pristine $ZrOX_2$, the Janus ZrOBrI possesses an intrinsic dipole with corresponding potential drops $\Delta\Phi$ (0.16 eV), which generates a built-in electric field EF (1.75 eV/Å) pointing from the I layer to the Br layer. The different carrier distributions will significantly affect the photocatalytic schemes of Janus semiconductors, which will be discussed below.

C. Photocatalytic properties

As an excellent water-splitting photocatalyst, apart from the proper band gap, the band-edge positions are required to straddle the redox potential of water. The absolute band-edge positions of VBM (E_{VBM}) and CBM (E_{CBM}) are extracted via the following formula [77,78]: $E_{VBM}^{abs} = E_{VBM}^{DFT} - V_{vac}$, $E_{CBM}^{abs} = E_{CBM}^{DFT} - V_{vac}$, where $E_{VBM/CBM}^{DFT}$ are the

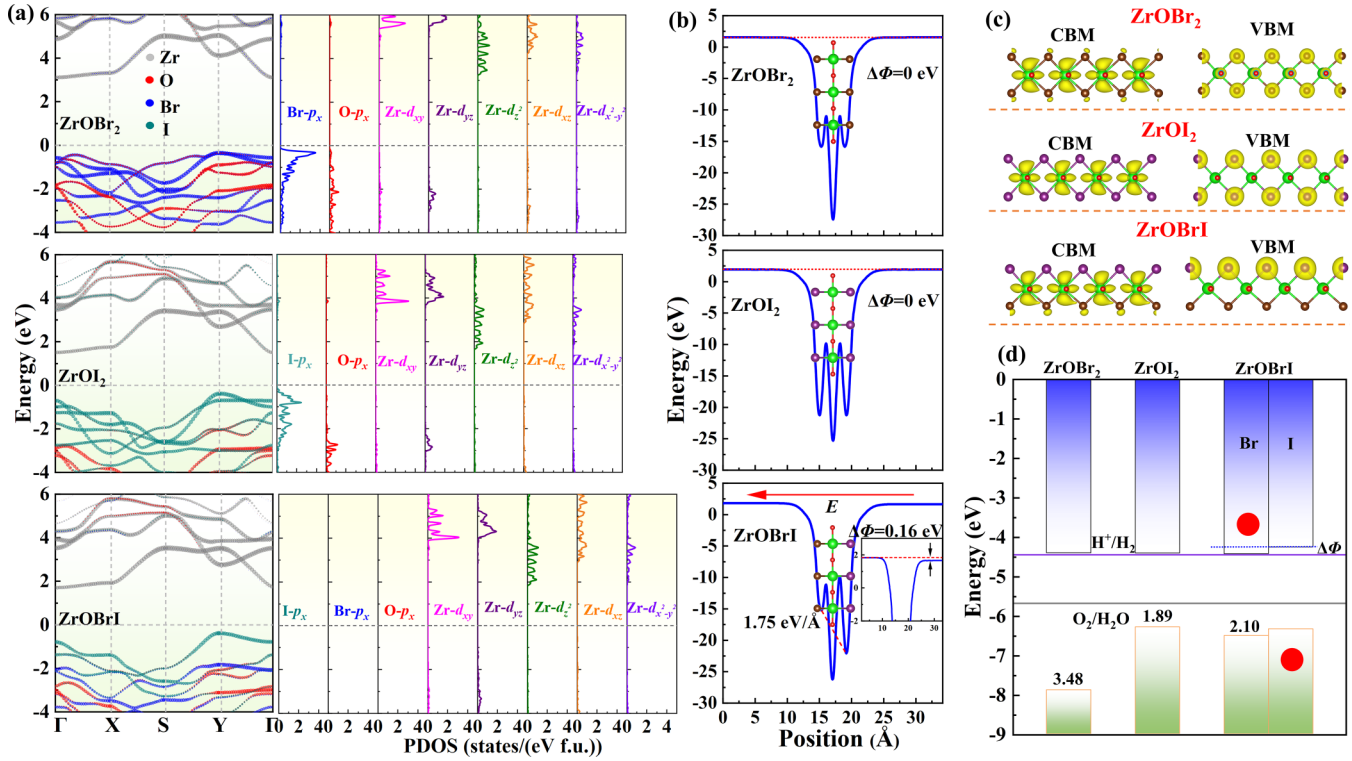

FIG. 2. (a) Projected band structures (left) and density of states (right) of the suborbitals of the Zr-d and -p_x orbitals of O/Br/I atoms calculated by the HSE06 method. (b) Plane-averaged electrostatic potential along the z direction. (c) The charge distribution of CBM and VBM states, the isosurface value is 0.03 e/Å^{-3}. (d) Band-edge alignments from the HSE06 method compared with the water redox potential at pH = 0. The red dots represent the real position of CBM and VBM.

energies of VBM/CBM calculated by the HSE06. For pristine $ZrOX_2$ without vertical EF, there is only one vacuum level, while for Janus ZrOBrI, there are two different vacuum levels [20]. First, as shown in Fig. 2(d), the pristine $ZrOX_2$ monolayers indeed meet the traditional photocatalytic mechanism [the VBM is lower than the oxidation potential of H_2O/O_2 (−5.67 eV) and the CBM is higher than the reduction potential of H^+/H_2 (−4.44 eV) at pH = 0], demonstrating their photocatalytic water-splitting potential. Second, for Janus ZrOBrI, it is necessary to identify the most possible schemes for photocatalytic HER and OER according to the different band edges on the different V_{vac} for the two surfaces [78]. Figure S5 (see the Supplemental Material [73]) shows four possible photocatalytic water-splitting schemes for Janus ZrOBrI. According to the charge distributions of VBM/CBM in Fig 2(c), we know that the most achievable scheme for the Janus ZrOBrI is the VBM relative to the small V_{vac} (I side) and the CBM relative to the big one (Br side) [red circles in Fig. 2(c)]. It can be found that the band-edge positions of Janus ZrOBrI can also cross the redox potential [Fig. 2(d)], implying it can satisfy the basic requirements for full water splitting. Furthermore, the band-edge positions calculated by the G_0W_0 are also presented in Fig. S6 in the Supplemental Material [73], and we can see that the redox capabilities of these monolayers are improved due to the enlarged band gaps. Since the band-gap values obtained by HSE06 are accurate enough and close to the experimental results, we only consider the HSE06 method in subsequent calculations of strained band structures to save computational resources. To be mentioned, it has been demonstrated that transition metal oxyhalides $NbOCl_2$ and $NbOI_2$ were unable to meet the band-edge requirement to achieve full photocatalytic water splitting at pH = 0 under the unstrained case [44], while the corresponding Janus NbOClI and NbOBrI were compatible with both HER and OER without considering optimal band-alignment mechanism [45].

Considering that materials may be affected by strain during operation in practical engineering applications, we investigated band gaps and band alignments of $ZrOX_2$ and Janus ZrOBrI monolayers under biaxial compressive strain (within −6%) [4,79,80]. As shown in Fig. 3(a), band gaps of all studied monolayers decreased monotonically with the increase of compressive strain. Furthermore, Fig. 3(b) shows

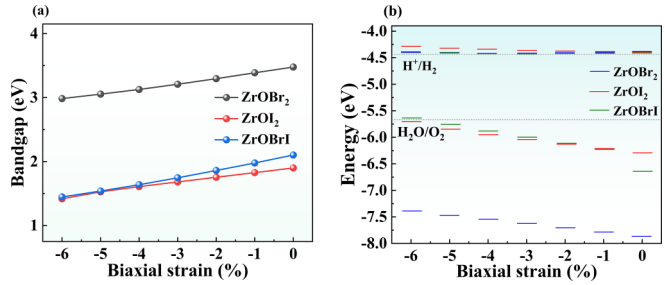

FIG. 3. (a) Biaxial compressive strain effect on the band gap of $ZrOX_2$ and Janus ZrOBrI monolayers at the HSE06 level. (b) Biaxial compressive strain effect on the band alignment of $ZrOX_2$ and Janus ZrOBrI monolayers at pH = 0.

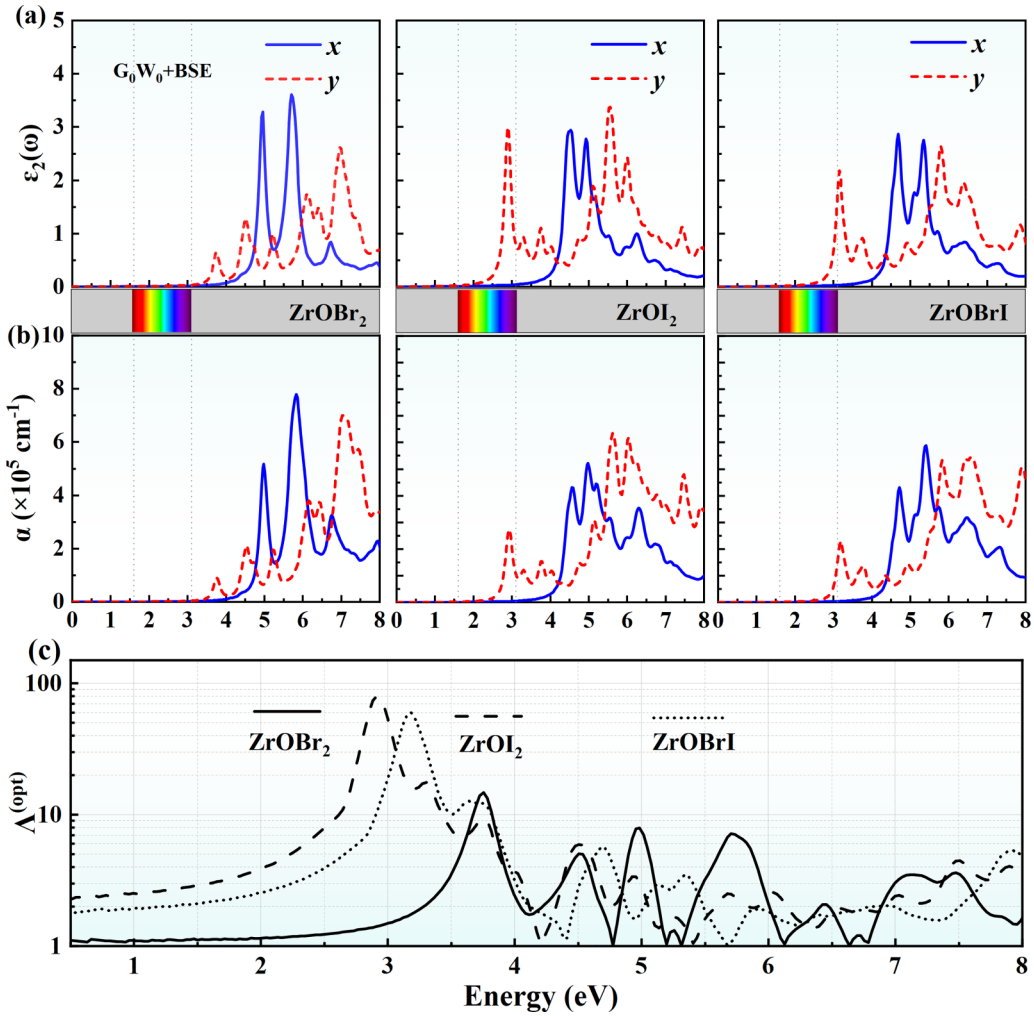

FIG. 4. (a) The imaginary parts of the dielectric function calculated by the G_0W_0 + BSE method for $ZrOX_2$ and Janus ZrOBrI monolayers, respectively. (b) The optical absorption coefficients computed by the G_0W_0 + BSE method for $ZrOX_2$ and Janus ZrOBrI monolayers. (c) The optical anisotropy ratio as a function of photon energy for $ZrOX_2$ and Janus ZrOBrI monolayers.

that all of these monolayers, except Janus ZrOBrI at −6%, could still meet the photocatalytic water splitting under biaxial strain in acidic conditions ($pH = 0$). As the compressive strain increased, the position of VBM gradually shifted towards the oxidation potential of H_2O/O_2, and the position of CBM in $ZrOBr_2$ and Janus ZrOBrI did not change significantly, but gradually moved upwards in $ZrOI_2$. Surprisingly, when the compressive strain reached −4%, the overpotential $\chi(H_2)$ and $\chi(O_2)$ (the potential difference between the reduction/oxidation potential and actual CBM/VBM) of $ZrOI_2$ exceeded 0.1 eV, indicating that there is enough energy for photogenerated carriers to proceed with the HER and OER [81,82]. To be mentioned, despite Janus ZrOBrI having an internal *EF*, its redox capacity was not enhanced due to the optimal band-alignment mechanism. In general, these studied systems can achieve photocatalytic water splitting under practical conditions in an acid environment.

D. Optical properties

Optical property is one of the golden keys to measuring whether semiconductor materials are excellent optoelectronic devices. Besides, photocatalysts with prominent light absorption will work more efficiently. Therefore, we studied the optical properties of the pristine $ZrOX_2$ and Janus ZrOBrI by computing the complex dielectric constants ε using the G_0W_0-BSE method. The absorption coefficient can be written as

$$\alpha(\omega) = \frac{\sqrt{2}\omega}{c}\left[\sqrt{\varepsilon_1^2(\omega) + \varepsilon_2^2(\omega)} - \varepsilon_1(\omega)\right]^{1/2}, \qquad (2)$$

where ε_1 and ε_2 represent the real and imaginary parts of the dielectric function, respectively. From Fig. 4(b), we find that the optical absorption spectra of these monolayers exhibit high anisotropy and strong linear optical dichroism between the *x*- and *y* directions. Interestingly, the optical absorption of *y*-polarized light is stronger than that of *x*-polarized light in the range of about 2 ∼ 4 and 6 ∼ 8 eV, while the opposite is true in the range of about 4.5 ∼ 5.5 eV. Besides, $ZrOBr_2$, $ZrOI_2$, and Janus ZrOBrI have significant optical absorption peaks along the *y* direction at energies of 3.75, 2.91, and 3.18 eV, respectively. Notably, Zr-d_{z^2} orbitals can hardly hybridize with the planar I/Br-p_x orbitals, while Zr-d_{xz} orbitals can effectively hybridize with I/Br-p_x orbitals;

thus, transitions from the I/Br-p_x valence bands to the Zr-d_{xz} conduction bands along the y direction are easier to achieve despite the Zr-d_{z^2} orbitals having lower conduction-band energy in the x direction [as shown in Fig. 2 (a)], which leads to effective light absorption of the incident light polarized along the b axis of these monolayers. Therefore, the strong optical anisotropy can be observed in the three systems. Compared to other semiconductors [4,83], the wide light absorption range (from visible to ultraviolet regions) and appreciable optical absorption coefficient ($\sim 10^5\ \mathrm{cm}^{-1}$) render $ZrOX_2$ and Janus ZrOBrI candidates for solar-conversion devices. In addition, such outstanding optical properties bring these three monolayers great advantages as ideal photocatalysts. Moreover, the exciton binding energies E_b of $ZrOBr_2$, $ZrOI_2$, and Janus ZrOBrI are calculated to be 1.34, 0.43, and 0.47 eV, respectively, which are comparable to those of photocatalysts such as GaN (0.44 eV) [84], GaInSSe (0.46 eV) [82], Al_2S_3 (1.09 eV) [85], and In_2Se_2 (0.69 eV) [85], indicating they can effectively split excitons into free electrons and holes.

The strong linear optical dichroism of $ZrOX_2$ and Janus ZrOBrI, derived from their anisotropic orbital hybridization, can be quantified as [86]

$$\Lambda^{(\mathrm{opt})}(\hbar\omega) = \frac{\max[\alpha_x(\hbar\omega, \alpha_y(\hbar\omega)]}{\min[\alpha_x(\hbar\omega, \alpha_y(\hbar\omega)]}, \tag{3}$$

where $\alpha_{x,y}$ $(\hbar\omega)$ is the absorption coefficient in the x/y direction at photon energy $\hbar\omega$. As shown in Fig. 4(c), since the incident optical light could hardly be absorbed in the x direction within the energy of about 3.5 eV, the three monolayers exhibited significant $\Lambda^{(\mathrm{opt})}$. Specifically, at the energy of 3.75, 2.91, and 3.18 eV, the maximum $\Lambda^{(\mathrm{opt})}$ were found to be 14.73, 80.78, and 59.82 for $ZrOBr_2$, $ZrOI_2$, and Janus ZrOBrI, respectively. Such unique optical characteristics provided a method to directly determine the crystal orientation using a polarization optical microscope. At around 500 nm, the $\Lambda^{(\mathrm{opt})}$ of $ZrOBr_2$, $ZrOI_2$, and Janus ZrOBrI were found to be 1.23, 7.39, and 3.89, respectively, which were comparable to or even larger than that of $PdSe_2$ ($\Lambda^{(\mathrm{opt})} = 1.09$) [87], GeSe ultrathin film ($\Lambda^{(\mathrm{opt})} = 1.09$) [86], transition metal oxyhalides $NbOI_2$ ($\Lambda^{(\mathrm{opt})} = 1.75$) [42], and corresponding Janus NbOXY (X/Y = Cl, Br, I) monolayers ($\Lambda^{(\mathrm{opt})} = 1.8 \sim 5.5$) [45]. The strong anisotropic optical absorption of $ZrOX_2$ and its Janus ZrOBrI monolayers indicated their great potential for applications in polarization-sensitive photonics fields, such as linear polarizers and polarization-dependent photodetectors.

E. Transport properties

Carrier mobility is a crucial factor in determining whether semiconductors are good candidates for electronic and optoelectronic devices. In addition, higher and direction-dependent carrier mobility is also favorable for semiconducting photocatalysts. Here, we evaluated the charge-migration ability of $ZrOX_2$ and Janus ZrOBrI monolayers using the DP theory [66,67]: $\mu_{2D} = \frac{e\hbar^3 C_{2D}}{k_B T m^* m_d E_1^2}$, where e, k_B, and T are the electron charge, Boltzmann constant, and temperature, respectively. C_{2D}, E_1, m^*, and m_d represent the elastic modulus, deformation potential constant, effective mass along the transport direction (x and y), and average effective mass ($m_d = \sqrt{m_x^* m_y^*}$), respectively. The calculated data of C_{2D}, E_1, m^*, and carrier mobility μ_{2D} are summarized in Table II, and the relevant fitted results are presented in Fig. S7 and Fig. S8 in the Supplemental Material [73].

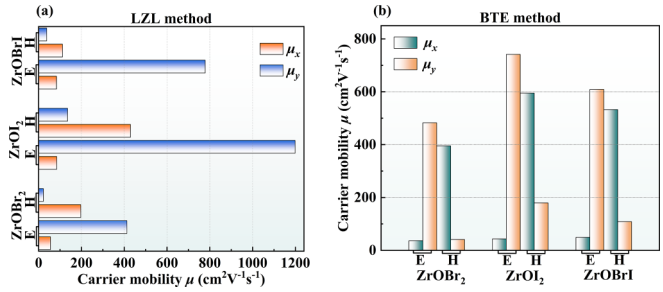

FIG. 5. (a) The anisotropic electron and hole mobility obtained by Lang-Zhang-Liu (LZL) method for $ZrOX_2$ and Janus ZrOBrI monolayers. (b) The anisotropic electron and hole mobility obtained by the Boltzmann transport equation (BTE) method for $ZrOX_2$ and Janus ZrOBrI monolayers.

The results showed that the carrier mobility μ_{2D} of electrons and holes in $ZrOX_2$ and Janus ZrOBrI monolayers was orientation-dependent due to anisotropic C_{2D}, E_1, and m^*. Interestingly, all of these monolayers possessed smaller electron-effective mass along the y direction and smaller hole-effective mass in the x direction, i.e. , $m_{ey}^* < m_{ex}^*$, $m_{hx}^* < m_{hy}^*$, where x/y represents the two orthogonal transport directions, and e/h signifies the two types of carriers. This phenomenon can be analyzed from the band structures. For all these monolayers, the conduction-band edge at the Γ point dispersed more sharply along the y direction (i.e., Γ → Y) while relatively flatter in the x direction (i.e., Γ→X), resulting in m_{ey}^* being one order of magnitude smaller than m_{ex}^*. The anisotropic hole-effective mass at the Y point could be analyzed similarly. Generally, the smaller the effective mass, the faster the carrier responded to the external field force. For electron mobility, all these compounds exhibited the anisotropy of $\mu_{ey} > \mu_{ex}$ due to the electron-effective mass anisotropy of $m_{ey}^* < m_{ex}^*$. For hole mobility, in the $ZrOBr_2$ monolayer, the hole-effective mass anisotropy of $m_{hx}^* < m_{hy}^*$ was sufficient to compensate for the deformation potential anisotropy of $E_{1hx} > E_{1hy}$, thus leading to the hole mobility anisotropy $\mu_{hx} > \mu_{hy}$. However, in monolayer $ZrOI_2$ and Janus ZrOBrI, the anisotropy of $m_{hx}^* < m_{hy}^*$ could not counteract the effect of more significant anisotropy of $E_{1hx} > E_{1hy}$; a reverse result of $\mu_{hx} < \mu_{hy}$ occurred in both materials.

In fact, for the same carrier in a semiconductor, the x- and y-directional deformation potentials (E_{1x} and E_{1y}) will couple together and jointly contribute to mobility. Lang, Zhang, and Liu (LZL) showed that based on the DP theory, the carrier mobility of 2D semiconductors with anisotropy is more precisely expressed as [88]

$$\mu_x = \frac{e\hbar^3\left(\frac{5C_{2D,x}+3C_{2D,y}}{8}\right)}{k_B T m_x^* m_d\left(\frac{9E_{1,x}^2+7E_{1,x}E_{1,y}+4E_{1,y}^2}{20}\right)}. \tag{4}$$

The μ_y could be acquired by replacing $x \to y$ in Eq. (4). As shown in Table II and Fig. 5(a), compared to the traditional DP of Bardeen and Shockley, the hole mobility in the LZL method

TABLE II. Elastic modulus (C_{2D}), deformation potential (E_1), effective mass (m^*), and carrier mobility (μ_{2D}) for pristine $ZrOX_2$ and Janus ZrOBrI monolayers along the x and y directions. The carrier mobility computed using the Lang-Zhang-Liu anisotropic method is displayed in the brackets.

Materials	Carrier types		C_{2D} (Nm^{-1})	m^* (m_e)	E_1 (eV)	μ_{2D} ($cm^2\,V^{-1}\,s^{-1}$)
$ZrOBr_2$	Electrons	x	86.06	3.80	2.23	80.02 (55.47)
		y	38.57	0.39	2.61	249.56 (412.76)
	Holes	x	86.06	0.43	4.42	150.90 (197.02)
		y	38.57	4.93	1.61	44.05 (22.14)
$ZrOI_2$	Electrons	x	98.72	3.79	2.58	81.87 (84.56)
		y	35.58	0.27	1.55	1140.74 (1198.82)
	Holes	x	98.72	0.35	5.80	286.76 (429.16)
		y	35.58	1.08	1.24	742.57 (135.18)
ZrOBrI	Electrons	x	93.23	4.05	1.81	132.41 (83.57)
		y	36.92	0.31	2.31	415.64 (778.52)
	Holes	x	93.23	0.37	9.58	74.29 (111.64)
		y	36.92	1.66	1.69	210.78 (37.62)

was significantly improved in the x direction while reduced in the y direction.

Furthermore, under the LZL method, all three monolayers presented a pattern: $m^*_{ey} < m^*_{ex}$, $\mu_{ey} > \mu_{ex}$; $m^*_{hx} < m^*_{hy}$, and $\mu_{hx} > \mu_{hy}$. This can be explained by the effective E_1, whose anisotropy is weakened by the formula $9E^2_{1,x} + 7E_{1,x}E_{1,y} + 4E^2_{1,y}$. The result showed that all these monolayers have relatively high electron mobility with values ranging from 412.76 to 1198.82 $cm^2\,V^{-1}\,s^{-1}$, which were comparable to or larger than those of common 2D semiconductors [15], such as MoSSe (530 $cm^2\,V^{-1}s^{-1}$) [15], ScSeCl (662.21 $cm^2\,V^{-1}\,s^{-1}$) [80], and AlSCl (716.62 $cm^2\,V^{-1}s^{-1}$) [4] monolayers, indicating $ZrOX_2$ and Janus ZrOBrI monolayers can be promising candidates for electronic and optoelectronic devices. Notably, the carrier transport properties of these materials we studied were very similar to those of transition metal oxyhalides $NbOX_2$ (X = Cl, Br, I) with high electron mobility in the y direction, up to $10^3\,cm^2\,V^{-1}\,s^{-1}$. However, the hole mobility of $ZrOX_2$ and Janus ZrOBrI is much higher than that of $NbOX_2$, which can be attributed to the heavy hole mass in $NbOX_2$ compounds [44]. Moreover, we also calculated the anisotropic ratio $R_{ani} = \max(\mu_x, \mu_y)/\min(\mu_x, \mu_y)$ to evaluate the anisotropy of carrier mobility, where $\max(\mu_x, \mu_y)$ and $\min(\mu_x, \mu_y)$ are the maximum and minimum carrier mobility for electrons and holes, respectively. The mobility anisotropic ratio R_{ani} of $ZrOBr_2$, $ZrOI_2$, and Janus ZrOBrI monolayers were calculated to be 7.44 (8.90), 14.18 (3.17), and 9.32 (2.97) for electrons (holes), respectively, which were larger than those of reported 2D semiconductors, such as Janus PtSSe [R_{ani} = 1.33(6.01)] [89], AlSI monolayer [R_{ani} = 4.02(1.29)] [4], and single-layer P_4O_2 [R_{ani} = 1.49(1.80)] [90]. Excitingly, the highly anisotropic transport properties of $ZrOX_2$ and Janus ZrOBrI can provide approaches for nanoelectronic device engineering. For example, by selectively arranging electrodes along different crystal directions, the carrier mobility can be increased by at least one order of magnitude [45]. Besides, orientation-dependent carrier mobility in these monolayers can reduce the recombination of photogenerated electron-hole pairs, which is beneficial to improving the performance of photocatalytic water splitting.

From Fig. 2(a), we can notice that the conduction bands of these three monolayers in the x direction were so flat they could not be regarded as parabolic shapes. Besides, there are several maxima whose energies are close to the VBM on the valence band in the $ZrOBr_2$ monolayer. Therefore, obtaining the effective mass of the carrier through parabolic fitting with band energy may not be accurate. Then, we further calculated the carrier transport properties by solving the BTE using the semiclassical Boltzmann theory, which considers all bands and regions in the BZ [91]. The calculated results are presented in Table III and Fig. S9 and Fig. S10 (see the Supplemental Material [73]). In this method, the calculated m^*_{ey}, m^*_{hx}, and m^*_{hy} were almost consistent with the results obtained from the DP method, while the obtained m^*_{ex} (5.45, 5.02, and 4.21 m_e for the $ZrOBr_2$, $ZrOI_2$, and Janus ZrOBrI monolayers, respectively) were much higher than those obtained from the DP method (3.80, 3.79, and 4.05 m_e for the $ZrOBr_2$, $ZrOI_2$, and Janus ZrOBrI monolayers, respectively) due to the nonparabolic conduction band. As shown in Fig. 5(b), carrier mobility obtained by the BTE method and LZL method followed similar regulars: (i) $\mu_{ey} > \mu_{ex}$, and $\mu_{hx} > \mu_{hy}$; (ii)

TABLE III. Carrier effective mass m^*_x/m^*_y and mobility μ_x/μ_y for $ZrOX_2$ and Janus ZrOBrI monolayers by the BTE method. These data were calculated at the PBE level with a carrier density of $10^{13}\,cm^{-2}$ and an assumption of τ = 10fs.

	$ZrOBr_2$	$ZrOI_2$	ZrOBrI
m^*_{ex} (m_e)	5.45	5.02	4.21
m^*_{ey} (m_e)	0.41	0.29	0.34
m^*_{hx} (m_e)	0.51	0.37	0.39
m^*_{hy} (m_e)	4.86	1.22	1.92
μ_{ex} ($cm^2\,V^{-1}\,s^{-1}$)	36.58	43.38	49.29
μ_{ey} ($cm^2\,V^{-1}\,s^{-1}$)	482.46	741.43	608.83
μ_{hx} ($cm^2\,V^{-1}\,s^{-1}$)	395.19	594.91	532.48
μ_{hx} ($cm^2\,V^{-1}\,s^{-1}$)	40.96	179.46	108.38

TABLE IV. The elastic constant coefficient C_{ij} (in N/m), piezoelectric tensors e_{ij} (in $\times 10^2$ pC/m), and piezoelectric strain coefficients d_{ij} (in pm/V) of 2D $ZrOX_2$ and Janus ZrOBrI monolayers.

Materials	C_{11}	C_{22}	C_{21}	C_{66}	e_{21}	e_{22}	e_{16}	e_{31}	e_{32}	d_{21}	d_{22}	d_{16}	d_{31}	d_{32}
$ZrOBr_2$	80.02	38.03	1.90	10.39	−19.68	1.61	−0.06	0	0	−24.71	5.47	−0.58	0	0
$ZrOI_2$	101.11	34.41	1.90	9.28	−23.78	0.37	−0.77	0	0	−23.56	2.38	−8.30	0	0
ZrOBrI	94.00	36.76	1.99	10.00	−22.05	0.69	−1.04	0.09	0.09	−23.53	3.09	−10.40	0.09	0.23

Strong anisotropy existed between electron and hole mobility in these three compounds; and (iii) the monolayer $ZrOI_2$ had the highest carrier mobility, while the Janus ZrOBrI possessed moderate carrier mobility. Since the BTE method for calculating the effective mass took into account all bands and regions in the Brillouin zone, we expect these data to show better agreement with experimental transport measurements.

F. Elastic and piezoelectric properties

For 2D monolayers without out-of-plane periodicity, elastic coefficients C_{ij} associated with the out-of-plane degree of freedom can be discarded. Considering the symmetry requirement of the orthorhombic *Pmm*2 space group in $ZrOX_2$ and *Pm* space group in Janus ZrOBrI, the in-plane C_{ij} can be expressed as

$$C_{ik} = \begin{pmatrix} C_{11} & C_{12} & 0 \\ C_{12} & C_{22} & 0 \\ 0 & 0 & C_{66} \end{pmatrix}. \quad (5)$$

The calculated results are summarized in Table IV. Combining these data, Young's modulus $Y(\theta)$ and Poisson's ratio $\nu(\theta)$ concerning the in-plane angle (θ) could be obtained using the following formulas [92]

$$Y(\theta) = \frac{C_{11}C_{22} - C_{12}^2}{C_{11}s^4 + \left(\frac{C_{11}C_{22}-C_{12}^2}{C_{66}} - 2C_{12}\right)s^2c^2 + C_{22}c^4}, \quad (6)$$

$$\nu(\theta) = \frac{C_{12}c^4 - \left(C_{11} + C_{12} - \frac{C_{11}C_{22}-C_{12}^2}{C_{66}}\right)c^2s^2 + C_{12}s^4}{C_{22}c^4 + \left(\frac{C_{11}C_{22}-C_{12}^2}{C_{66}} - 2C_{12}\right)c^2s^2 + C_{11}s^4}, \quad (7)$$

where s and c denote sin (θ) and cos (θ), respectively. The orientation-dependent $Y(\theta)$ and ν (θ) are depicted in Figs. 6(a) and 6(b). It can be observed that both $Y(\theta)$ and ν (θ) in these three monolayers exhibited strong anisotropy. Besides, Young's modulus along the x and y directions, namely, Y_x (Y_y), were 79.93 (37.98), 101.01 (34.37), and 93.89(36.72) N m^{-1} for $ZrOBr_2$, $ZrOI_2$, and ZrOBrI, respectively, showing that the $ZrOI_2$ monolayer was the most stiff, whereas the $ZrOBr_2$ monolayer was the most flexible. Poisson's ratio of $ZrOX_2$ and Janus ZrOBrI was entirely positive with values ranging from 0.05 to 0.50. Young's modulus of $ZrOX_2$ and Janus ZrOBrI were smaller than previously reported graphene (342.2 N m^{-1}) [74], hexagonal boron nitride (275.8 N m^{-1}) [74], and h-TiS_2 (167 N m^{-1}) [93], indicating that these calculated monolayers have excellent mechanical flexibility and will be used in flexible electronic applications.

Due to the breaking of spatial inversion symmetry, $ZrOX_2$ and Janus ZrOBrI monolayers exhibited piezoelectric effects. The piezoelectric tensor e_{ik} and piezoelectric coefficient d_{ij} in the 2D materials could be connected by the Voigt notation: $e_{ik} = d_{ij}C_{jk}$. Considering the symmetry, the e_{ik} and d_{ij} of studied monolayers could be simplified as

$$e_{ik} = \begin{pmatrix} 0 & 0 & e_{16} \\ e_{21} & e_{22} & 0 \\ e_{31} & e_{32} & 0 \end{pmatrix}, \quad d_{ij} = \begin{pmatrix} 0 & 0 & d_{16} \\ d_{21} & d_{22} & 0 \\ d_{31} & d_{32} & 0 \end{pmatrix}, \quad (8)$$

where $d_{21} \neq d_{22}$ and $d_{31} \neq d_{32}$ denote two distinctive in-plane and out-of-plane piezoelectric coefficients, respectively, and d_{16} means the shear piezoelectric coefficient. The corresponding schematic diagram is shown in Fig. 6(c), and the calculated results are tabulated in Table IV. It can be observed that all these monolayers had an ideal in-plane transverse piezoelectric coefficient d_{21}, which were −24.71, −23.56, and −23.53 pm/V for $ZrOBr_2$, $ZrOI_2$, and Janus ZrOBrI, respectively. The negative value meant that the polarization in the y-axis direction would weaken when stretching the x axis of the crystal. Additionally, attributed to the anisotropic crystal structure and elastic response, there was a strong anisotropy between in-plane transverse and in-plane longitude piezoelectric coefficients. Typically, the $ZrOI_2$ had the strongest anisotropy with an anisotropic ratio of about 9.9 (d_{21}/d_{22}). Interestingly, unlike other 2D transition metal oxyhalides MOX_2, whose piezoelectric response was mainly composed of in-plane longitudinal piezoelectric coefficients, such as $NbOX_2$ (X = Cl, Br, I) (d_{11}: 27.4 ∼ 42.2 pm/V and d_{12}: −5.1 ∼ −4.1 pm/V) [43], $TiOX_2$ (X = Cl, Br) (d_{11}: 33.8 ∼ 37.6 pm/V and d_{12}:−3.8 ∼−3.7 pm/V) [40], and FM VOX_2 (X = F, Cl, Br) (d_{11}: 29 ∼ 29.6 pm/V and d_{12}: −0.75 ∼ 0.24 pm/V) monolayers [40], $ZrOX_2$ and Janus ZrOBrI with considerable negative transverse piezoelectric response were unique and could be preferred piezoelectric materials. This could be attributed to the polar displacement of the Zr cation along the y axis, which led to the bending of the O–M–O bonding chain in the x axis of the crystal. Once the tensile mechanical strain was applied along the x axis, the angle of O-M-O bonding decreased towards 180º, thus greatly reducing polarization along the y direction. Surprisingly, the Janus ZrOBrI also had out-of-plane piezoelectric coefficients d_{31} and d_{32} due to the inversion asymmetry along the z direction. The d_{31} of Janus ZrOBrI (0.09 pm/V) was superior to typical 2D piezoelectric materials like Janus $NbOXY$ (X/Y = Cl, Br, I) (0.002 ∼ 0.074 pm/V) [45] and Janus MoSTe (0.03 pm/V) [32] monolayers. Besides, the d_{32} was larger than d_{31}, with a value of 0.24 pm/V. With both large in-plane d_{21} and significant out-of-plane d_{32} piezoelectric coefficients, the particularly special 2D semiconductor ZrOBrI would be an excellent anisotropic piezoelectric candidate.

Since vertical piezoelectricity can be significantly improved by stacking [32,94], we investigated the piezoelectric

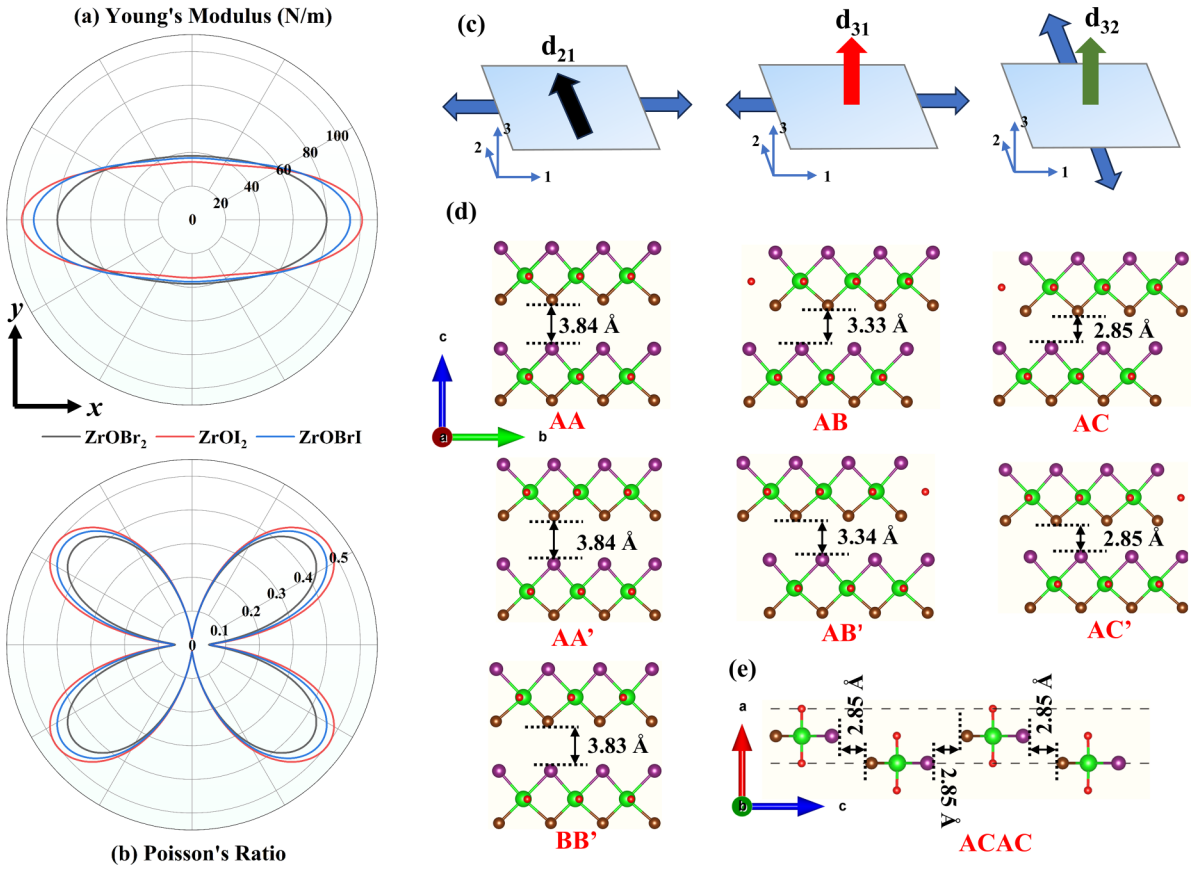

FIG. 6. The direction-dependent Young's modulus (a) and Poisson's ratio (b). The schematic diagram of piezoelectric responses (c), where the blue thin arrows represent the direction of mechanical stress and the thick arrows (black, red, and green) denote the direction of charge polarization. (d) Seven high-symmetry stacking types of bilayer Janus ZrOBrI. For AA, AB, and AC stacking, the two Janus ZrOBrI monolayers are parallelly orientated. Br and I atoms in up layers are settled on the I-top site (AA), on the Zr-top site (AB), and on the O-top site (AC). For AA′, AB′, and AC′ stacking, the two Janus ZrOBrI monolayers are antiparallelly orientated. Br and I atoms in up layers are settled on the I-top site (AA′), on the Zr-top site (AB′), and on the O-top site (AC′). The BB′ stacking represents Zr atoms in the upper layer settled on the top of Zr atoms in the lower layer. (e) Four-layer Janus ZrOBrI under the AC stacking mode.

response of multilayer Janus ZrOBrI. As shown in Fig. 6(d), seven different stacking models with high symmetry were considered to ascertain the energetically advantageous configuration, and the total energy of their system is shown in Table S2 in the Supplemental Material [73]. Obviously, the bilayer 2D Janus ZrOBrI structure stacked by AC mode is the most stable, with an interlayer distance of 2.85 Å and a binding energy of 0.24 eV. Subsequently, we computed the piezoelectric coefficients of multilayer Janus ZrOBrI stacked in AC mode. As shown in Table S3 (see the Supplemental Material [73]) and Fig. 7, elastic tensor (C_{21} and C_{22}) and piezoelectric tensor (e_{21}, e_{22}, e_{31}, and e_{32}) of multilayer 2D Janus ZrOBrI increased to varying degrees with the increase of the number of layers. Especially for the four-layer 2D Janus ZrOBrI, whose d_{31} and d_{32} reach 1.17 and 4.61 pm/V, respectively. Surprisingly, the growth rates of d_{31} and d_{32} in the four-layer reached 1200 and 1904%, respectively, significantly higher than that of four-layer 2D $LiAlTe_2$ (242%) [95]. This is because multilayer 2D Janus ZrOBrI was stacked by each Janus ZrOBrI monolayer with the same polarization direction, resulting in the superposition of out-of-plane dipole moments in multilayers. Although the elastic constants increased with increasing number of layers, the increase of e_{31} and e_{32} was greater, resulting in the increase of d_{31} and d_{32}. The vertical piezoelectric coefficient d_{32} of multilayer Janus ZrOBrI stacked in AC mode was close to AlN ($d_{33} = 5.1$ pm/V) [33] and $LiAlTe_2$ ($d_{31} = 2.76 \sim 3.32$ pm/V) [95], indicating that it could provide large out-of-plane piezoelectric output signals for device applications.

IV. CONCLUSIONS

In summary, based on first-principle calculations, we demonstrated that $ZrOX_2$ (X = Br, I) and Janus ZrOBrI monolayers are stable and mechanically flexible 2D semiconductors with excellent electronic, photocatalytic, optical, and piezoelectric properties. All of these monolayers have an indirect band gap (ranging from 1.89 to 3.48 eV), and their CBM and VBM can straddle the redox potential of water in acid environment (pH = 0), which means they can meet the prerequisite for photocatalytic water splitting. Furthermore, the effects of biaxial compressive strain (within -6%) on the band alignments and band gaps were also discussed. The results show that with the increase of strain, both CBM and

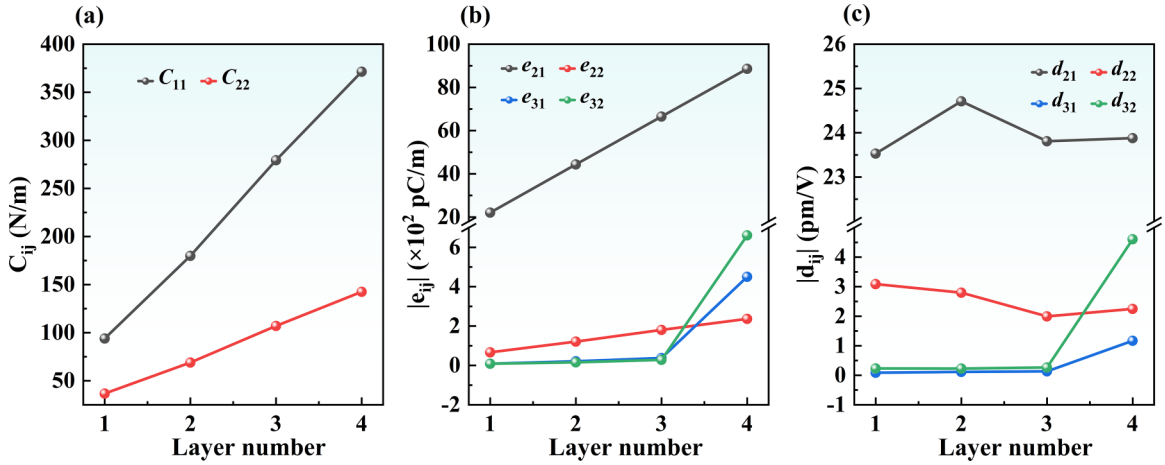

FIG. 7. (a)–(c) The relationship between the elastic tensor, piezoelectric tensor, and piezoelectric coefficients with the number of layers in multilayer ZrOBrI under AC mode.

VBM gradually shift toward higher energy. Because VBM is more sensitive to strain, the band gaps decrease monotonically with the increase of external strain. In addition, all three monolayers can still cross the redox potential of water under different strains. In particular, $ZrOI_2$ at -4% strain is the most ideal photocatalyst due to the sizable $\chi(H_2)$ and $\chi(O_2)$.

What is more, $ZrOX_2$ and Janus ZrOBrI exhibit outstanding optical absorption in the visible and ultraviolet regions, which makes them excellent solar collectors. Besides, the orientation-dependent optical properties also render them promising optical devices such as polarizers. Interestingly, all three systems have ultrahigh electron mobility in the y direction (reaching $10^2 \sim 10^3\,\mathrm{cm^2\,V^{-1}\,s^{-1}}$), indicating they are good electronic devices. Moreover, the anisotropy of carrier transport facilitates the separation of electrons and holes, thus improving the performance of photocatalytic water splitting. When it comes to piezoelectric properties, all systems exhibit exceptional in-plane transverse piezoelectric coefficients with a value of about 20 pm/V. Especially, for Janus ZrOBrI, there are two unique out-of-plane piezoelectric responses due to the broken symmetry of structure. In the AC stacking mode, the vertical piezoelectric coefficients d_{31} and d_{32} reach 1.17 and 4.61 pm/V, respectively, close to the 3D AlN ($d_{33} = 5.1\mathrm{pm/V}$). Our findings revealed that $ZrOX_2$ and Janus ZrOBrI monolayers are potential multifunctional 2D semiconductors with excellent performance in the fields of electronics, photocatalysis, optoelectronics, and piezoelectricity. We hope this research will provide theoretical guidance for further scientific exploration of 2D transition metal oxyhalides.

ACKNOWLEDGMENTS

This work was supported by the National Natural Science Foundation of China (Grant No. 12074274). Q.Y. was responsible for investigation, methodology, and writing the paper (original draft; review and editing); D.W. was responsible for methodology and writing the paper (original draft; review and editing); Z.-Y.Z. was responsible for visualization and supervision; H.-Y.G. was responsible for project administration and software; and X.-R.C. was responsible for visualization, supervision, and project administration.

The authors have no conflicts of interest to declare.

[1] A. Fujishima and K. Honda, Electrochemical photolysis of water at a semiconductor electrode, Nature (London) **238**, 37 (1972).

[2] Y. Ji, M. Yang, H. Lin, T. Hou, L. Wang, Y. Li, and S.-T. Lee, Janus structures of transition metal dichalcogenides as the heterojunction photocatalysts for water splitting, J. Phys. Chem. C **122**, 3123 (2018).

[3] S. Cao, J. Low, J. Yu, and M. Jaroniec, Polymeric photocatalysts based on graphitic carbon nitride, Adv. Mater. **27**, 2150 (2015).

[4] L. Pan, T. Zhang, C.-E. Hu, X.-R. Chen, and H.-Y. Geng, Two-dimensional AlXY (X = S, Se, and Y = Cl, Br, I) monolayers: Promising photocatalysts for water splitting with high-anisotropic carrier mobilities, J. Mater. Chem. A **10**, 22676 (2022).

[5] K. S. Novoselov, A. K. Geim, S. V. Morozov, D. Jiang, Y. Zhang, S. V. Dubonos, I. V. Grigorieva, and A. A. Firsov, Electric field effect in atomically thin carbon films, Science **306**, 666 (2004).

[6] S. Das, J. A. Robinson, M. Dubey, H. Terrones, and M. Terrones, Beyond Graphene: Progress in novel two-dimensional materials and van der Waals solids, Ann. Rev. Mater. Res. **45**, 1 (2015).

[7] K. S. Novoselov, D. Jiang, F. Schedin, T. J. Booth, V. V. Khotkevich, S. V. Morozov, and A. K. Geim, Two-dimensional atomic crystals, Proc. Natl. Acad. Sci. USA **102**, 10451 (2005).

[8] G. R. Bhimanapati, Z. Lin, V. Meunier, Y. Jung, J. Cha, S. Das, D. Xiao, Y. Son, M. S. Strano, V. R. Cooper *et al.*, Recent

advances in two-dimensional materials beyond graphene, ACS Nano **9**, 11509 (2015).

[9] C. Tan, X. Cao, X. J. Wu, Q. He, J. Yang, X. Zhang, J. Chen, W. Zhao, S. Han, G. H. Nam *et al.*, Recent advances in ultrathin two-dimensional nanomaterials, Chem. Rev. **117**, 6225 (2017).

[10] S. Manzeli, D. Ovchinnikov, D. Pasquier, O. V. Yazyev, and A. Kis, 2D transition metal dichalcogenides, Nat. Rev. Mater. **2**, 17033 (2017).

[11] A. K. Singh, K. Mathew, H. L. Zhuang, and R. G. Hennig, Computational screening of 2D materials for photocatalysis, J. Phys. Chem. Lett. **6**, 1087 (2015).

[12] S. Dervin, D. D. Dionysiou, and S. C. Pillai, 2D nanostructures for water purification: Graphene and beyond, Nanoscale **8**, 15115 (2016).

[13] M. R. Ashwin Kishore, A. O. Sjåstad, and P. Ravindran, Influence of hydrogen and halogen adsorption on the photocatalytic water splitting activity of C_2N monolayer: A first-principles study, Carbon **141**, 50 (2019).

[14] A. Kudo and Y. Miseki, Heterogeneous photocatalyst materials for water splitting, Chem. Soc. Rev. **38**, 253 (2009).

[15] X. Ma, X. Wu, H. Wang, and Y. Wang, A Janus MoSSe monolayer: A potential wide solar-spectrum water-splitting photocatalyst with a low carrier recombination rate, J. Mater. Chem. A **6**, 2295 (2018).

[16] W.-J. Ong, L.-L. Tan, Y. H. Ng, S.-T. Yong, and S.-P. Chai, Graphitic carbon nitride ($g-C_3N_4$)-based photocatalysts for artificial photosynthesis and environmental remediation: Are we a step closer to achieving sustainability? Chem. Rev. **116**, 7159 (2016).

[17] Z. Guo, J. Zhou, L. Zhu, and Z. Sun, MXene: A promising photocatalyst for water splitting, J. Mater. Chem. A **4**, 11446 (2016).

[18] J. He, L. Chen, F. Wang, Y. Liu, P. Chen, C. T. Au, and S. F. Yin, CdS nanowires decorated with ultrathin MoS_2 nanosheets as an efficient photocatalyst for hydrogen evolution, ChemSusChem **9**, 624 (2016).

[19] W. Choi, N. Choudhary, G. H. Han, J. Park, D. Akinwande, and Y. H. Lee, Recent development of two-dimensional transition metal dichalcogenides and their applications, Mater. Today **20**, 116 (2017).

[20] X. Li, Z. Li, and J. Yang, Proposed photosynthesis method for producing hydrogen from dissociated water molecules using incident near-infrared light, Phys. Rev. Lett. **112**, 018301 (2014).

[21] A. Y. Lu, H. Zhu, J. Xiao, C. P. Chuu, Y. Han, M. H. Chiu, C. C. Cheng, C. W. Yang, K. H. Wei, Y. Yang *et al.*, Janus monolayers of transition metal dichalcogenides, Nat. Nanotechnol. **12**, 744 (2017).

[22] A. Huang, W. Shi, and Z. Wang, Optical properties and photocatalytic applications of two-dimensional Janus Group-III monochalcogenides, J. Phys. Chem. C **123**, 11388 (2019).

[23] A. Bafekry, M. Faraji, M. M. Fadlallah, H. R. Jappor, N. N. Hieu, M. Ghergherehchi, and D. Gogova, Ab-initio-driven prediction of puckered penta-like PdPSeX (X = O, S, Te) Janus monolayers: Study on the electronic, optical, mechanical and photocatalytic properties, Appl. Surf. Sci. **582**, 152356 (2022).

[24] G. Yuan, X. Ma, J. Liao, T. Xie, Q. Xie, and Z. Yuan, First-principles calculations of 2D Janus $WSSiN_2$ monolayer for photocatalytic water splitting, ACS Appl. Nano Mater. **6**, 1956 (2023).

[25] S. Soleimani-Amiri, N. Ghobadi, A. Rezavand, and S. G. Rudi, First-principles prediction of two-dimensional Janus $XM\mathrm{In}Z_2$ (X = Cl, Br, I; M = Mg, Ca; and Z = S, Se, and Te) with promising spintronic and photocatalytic properties, Appl. Surf. Sci. **623**, 157020 (2023).

[26] H. Cai, Y. Guo, H. Gao, and W. Guo, Tribo-piezoelectricity in Janus transition metal dichalcogenide bilayers: A first-principles study, Nano Energy **56**, 33 (2019).

[27] W. Wu, L. Wang, Y. Li, F. Zhang, L. Lin, S. Niu, D. Chenet, X. Zhang, Y. Hao, T. F. Heinz *et al.*, Piezoelectricity of single-atomic-layer MoS_2 for energy conversion and piezotronics, Nature (London) **514**, 470 (2014).

[28] S.-B. Chen, Z.-Y. Zeng, X.-R. Chen, and X.-X. Yao, Strain-induced electronic structures, mechanical anisotropy, and piezoelectricity of transition-metal dichalcogenide monolayer CrS_2, J. Appl. Phys. **128**, 125111 (2020).

[29] K.-A. N. Duerloo, M. T. Ong, and E. J. Reed, Intrinsic piezoelectricity in two-dimensional materials, J. Phys. Chem. Lett. **3**, 2871 (2012).

[30] K. H. Michel and B. Verberck, Theory of elastic and piezoelectric effects in two-dimensional hexagonal boron nitride, Phys. Rev. B **80**, 224301 (2009).

[31] M. Zelisko, Y. Hanlumyuang, S. Yang, Y. Liu, C. Lei, J. Li, P. M. Ajayan, and P. Sharma, Anomalous piezoelectricity in two-dimensional graphene nitride nanosheets, Nat. Commun. **5**, 4284 (2014).

[32] L. Dong, J. Lou, and V. B. Shenoy, Large in-plane and vertical piezoelectricity in Janus transition metal dichalchogenides, ACS Nano **11**, 8242 (2017).

[33] C. M. Lueng, H. L. W. Chan, C. Surya, and C. L. Choy, Piezoelectric coefficient of aluminum nitride and gallium nitride, J. Appl. Phys. **88**, 5360 (2000).

[34] N. Ghobadi, S. Gholami Rudi, and S. Soleimani-Amiri, Electronic, spintronic, and piezoelectric properties of new Janus ZnAXY (A = Si, Ge, Sn, and X, Y = S, Se, Te) monolayers, Phys. Rev. B **107**, 075443 (2023).

[35] D. Bezzerga, E. A. Haidar, C. Stampfl, A. Mir, and M. Sahnoun, Ferro-piezoelectricity in emerging Janus monolayer BMX_2 (M = Ga, In and X = S, Se): Ab initio investigations, Nanoscale Adv. **5**, 1425 (2023).

[36] P. Wang, H. Liu, Y. Zong, H. Wen, J.-B. Xia, and H.-B. Wu, Two-dimensional In_2X_2X' (X and X′ = S, Se, and Te) monolayers with an intrinsic electric field for high-performance photocatalytic and piezoelectric applications, ACS Appl. Mater. Interfaces **13**, 34178 (2021).

[37] J. Zhao, W. Wu, J. Zhu, Y. Lu, B. Xiang, and S. A. Yang, Highly anisotropic two-dimensional metal in monolayer $MoOCl_2$, Phys. Rev. B **102**, 245419 (2020).

[38] G. Song, C. Zhang, T. Xie, Q. Wu, B. Zhang, X. Huang, Z. Li, G. Li, and B. Gao, Intrinsic ferromagnetism and the quantum anomalous Hall effect in two-dimensional $MnOCl_2$ monolayers, Phys. Chem. Chem. Phys. **24**, 20530 (2022).

[39] Y. Zhang, L.-F. Lin, A. Moreo, T. A. Maier, G. Alvarez, and E. Dagotto, Strongly anisotropic electronic and magnetic structures in oxide dichlorides $RuOCl_2$ and $OsOCl_2$, Phys. Rev. B **105**, 174410 (2022).

[40] M. Noor-A-Alam and M. Nolan, Large piezoelectric response in ferroelectric/multiferroelectric metal oxyhalide MOX_2 (M = Ti, V and X = F, Cl and Br) monolayers, Nanoscale **14**, 11676 (2022).

[41] R. Song, B.-L. Wang, K. Feng, J. Yao, and X. Li, Effect of stress regulation on electronic structure and optical properties of $TiOCl_2$ monolayer, Acta Phys. Sin. **71**, 077101 (2022).

[42] Y. Fang, F. Wang, R. Wang, T. Zhai, and F. Huang, 2D $NbOI_2$: A chiral semiconductor with highly in-plane anisotropic electrical and optical properties, Adv. Mater. **33**, 2101505 (2021).

[43] Y. Wu, I. Abdelwahab, K. C. Kwon, I. Verzhbitskiy, L. Wang, W. H. Liew, K. Yao, G. Eda, K. P. Loh, L. Shen *et al.*, Data-driven discovery of high performance layered van der Waals piezoelectric $NbOI_2$, Nat. Commun. **13**, 1884 (2022).

[44] L. Pan, Y.-L. Wan, Z.-Q. Wang, H.-Y. Geng, and X.-R. Chen, Two-dimensional anisotropic monolayers $NbOX_2$ (X = Cl, Br, I): Promising candidates for photocatalytic water splitting with high solar-to-hydrogen efficiency, J. Appl. Phys. **134**, 085105 (2023).

[45] T. Su, C. H. Lee, S.-D. Guo, G. Wang, W.-L. Ong, L. Cao, W. Zhao, S. A. Yang, and Y. S. Ang, 2D Janus niobium oxydihalide NbOXY: Multifunctional piezoelectric semiconductor for electronics, photonics, sensing and sustainable energy applications, Mater. Today Phys. **31**, 101001 (2023).

[46] G. Kresse and J. Furthmuller, Efficient iterative schemes for ab initio total-energy calculations using a plane-wave basis set, Phys. Rev. B **54**, 11169 (1996).

[47] G. Kresse and J. Hafner, Ab initio molecular dynamics for open-shell transition metals, Phys. Rev. B **48**, 13115 (1993).

[48] G. Kresse and J. Hafner, Norm-conserving and ultrasoft pseudopotentials for first-row and transition-elements, J. Phys.: Condens. Matter **6**, 8245 (1994).

[49] L. J. Sham and M. Schlüter, Density-functional theory of the band gap, Phys. Rev. B **32**, 3883 (1985).

[50] P. E. Blochl, Projector augmented-wave method, Phys. Rev. B **50**, 17953 (1994).

[51] J. P. Perdew, K. Burke, and Y. Wang, Generalized gradient approximation for the exchange-correlation hole of a many-electron system, Phys. Rev. B **54**, 16533 (1996).

[52] G. Kresse and D. Joubert, From ultrasoft pseudopotentials to the projector augmented-wave method, Phys. Rev. B **59**, 1758 (1999).

[53] J. P. Perdew, K. Burke, and M. Ernzerhof, Generalized gradient approximation made simple, Phys. Rev. Lett. **77**, 3865 (1996).

[54] S. Grimme, J. Antony, S. Ehrlich, and H. Krieg, A consistent and accurate ab initio parametrization of density functional dispersion correction (DFT-D) for the 94 elements H-Pu, J. Chem. Phys. **132**, 154104 (2010).

[55] S. Grimme, S. Ehrlich, and L. Goerigk, Effect of the damping function in dispersion corrected density functional theory, J .Comput. Chem. **32**, 1456 (2011).

[56] J. Neugebauer and M. Scheffler, Adsorbate-substrate and adsorbate-adsorbate interactions of Na and K adlayers on Al (111), Phys. Rev. B **46**, 16067 (1992).

[57] A. Togo and I. Tanaka, First principles phonon calculations in materials science, Scr. Mater. **108**, 1 (2015).

[58] J. Heyd, G. E. Scuseria, and M. Ernzerhof, Hybrid functionals based on a screened Coulomb potential, J. Chem. Phys. **118**, 8207 (2003).

[59] J. Heyd, G. E. Scuseria, and M. Ernzerhof, Erratum: Hybrid functionals based on a screened Coulomb potential, J. Chem. Phys. **124**, 219906(E) (2006).

[60] M. Shishkin and G. Kresse, Implementation and performance of the frequency-dependent GW method within the PAW framework, Phys. Rev. B **74**, 035101 (2006).

[61] L. Hedin, New method for calculating the one-particle Green's function with application to the electron-gas problem, Phys. Rev. **139**, A796 (1965).

[62] M. S. Hybertsen and S. G. Louie, Electron correlation in semiconductors and insulators: Band gaps and quasiparticle energies, Phys. Rev. B **34**, 5390 (1986).

[63] A. A. Mostofi, J. R. Yates, G. Pizzi, Y.-S. Lee, I. Souza, D. Vanderbilt, and N. Marzari, An updated version of WANNIER90: A tool for obtaining maximally-localised Wannier functions, Comput. Phys. Commun. **185**, 2309 (2014).

[64] K. Kutorasinski, B. Wiendlocha, J. Tobola, and S. Kaprzyk, Importance of relativistic effects in electronic structure and thermopower calculations for Mg_2Si, Mg_2Ge, and Mg_2Sn, Phys. Rev. B **89**, 115205 (2014).

[65] E. E. Salpeter and H. A. Bethe, A relativistic equation for bound-state problems, Phys. Rev. **84**, 1232 (1951).

[66] J. Bardeen and W. Shockley, Deformation potentials and mobilities in non-polar crystals, Phys. Rev. **80**, 72 (1950).

[67] S. Bruzzone and G. Fiori, Ab-initio simulations of deformation potentials and electron mobility in chemically modified graphene and two-dimensional hexagonal boron-nitride, Appl. Phys. Lett. **99**, 222108 (2011).

[68] G. K. H. Madsen and D. J. Singh, BoltzTraP. A code for calculating band-structure dependent quantities, Comput. Phys. Commun. **175**, 67 (2006).

[69] S. P. Ong, W. D. Richards, A. Jain, G. Hautier, M. Kocher, S. Cholia, D. Gunter, V. L. Chevrier, K. A. Persson, and G. Ceder, Python Materials Genomics (pymatgen): A robust, open-source python library for materials analysis, Comput. Mater. Sci. **68**, 314 (2013).

[70] S. Baroni, S. de Gironcoli, A. Dal Corso, and P. Giannozzi, Phonons and related crystal properties from density-functional perturbation theory, Rev. Mod. Phys. **73**, 515 (2001).

[71] M. N. Blonsky, H. L. Zhuang, A. K. Singh, and R. G. Hennig, Ab initio prediction of piezoelectricity in two-dimensional materials, ACS Nano **9**, 9885 (2015).

[72] N. Yang, G. Gou, X. Lu, and Y. Hao, Linear dichroism and polarization controllable persistent spin helix in two-dimensional ferroelectric $ZrOI_2$ monolayer, Nano Res. **15**, 6779 (2022).

[73] See Supplemental Material at http://link.aps.org/supplemental/10.1103/PhysRevB.109.035411 for additional calculations and analyses. It also contains Ref. [96].

[74] R. C. Andrew, R. E. Mapasha, A. M. Ukpong, and N. Chetty, Mechanical properties of graphene and boronitrene, Phys. Rev. B **85**, 125428 (2012).

[75] M. Sun and U. Schwingenschlögl, B_2P_6: A two-dimensional anisotropic Janus material with potential in photocatalytic water splitting and metal-ion batteries, Chem. Mat. **32**, 4795 (2020).

[76] M. Sun, Y. Luo, Y. Yan, and U. Schwingenschlögl, Ultrahigh carrier mobility in the two-dimensional semiconductors B_8Si_4, B_8Ge_4, and B_8Sn_4, Chem. Mat. **33**, 6475 (2021).

[77] H.-Y. Liu, C.-L. Yang, M.-S. Wang, and X.-G. Ma, Two-dimensional BiP_3 with high carrier mobility and moderate band gap for hydrogen generation from water splitting, Appl. Surf. Sci. **501**, 144263 (2020).

[78] N.-H. Qiao, C.-L. Yang, M.-S. Wang, and X.-G. Ma, Two-dimensional TeX (X = C, Si, Ge) monolayers with strong

intrinsic electric field for efficiency hydrogen evolution reaction, Surf. Interfaces **31**, 102011 (2022).

[79] V. M. Pereira and A. H. Castro Neto, Strain engineering of graphene's electronic structure, Phys. Rev. Lett. **103**, 046801 (2009).

[80] F. Y. Xu, Y. Zhou, T. Zhang, Z. Y. Zeng, X. R. Chen, and H. Y. Geng, An ab initio study of two-dimensional anisotropic monolayers ScXY (X = S and Se; Y = Cl and Br) for photocatalytic water splitting applications with high carrier mobilities, Phys. Chem. Chem. Phys. **24**, 3770 (2022).

[81] J. Wang, J. Lu, X. Zhao, G. Hu, X. Yuan, and J. Ren, Two-dimensional Janus AsXY (X = Se, Te; Y = Br, I) monolayers for photocatalytic water splitting, Eur. Phys. J. B **96**, 17 (2023).

[82] P. Wang, Y. Zong, H. Liu, H. Wen, H.-B. Wu, and J.-B. Xia, Highly efficient photocatalytic water splitting and enhanced piezoelectric properties of 2D Janus group-III chalcogenides, J. Mater. Chem. C **9**, 4989 (2021).

[83] X. Lv, L. Yu, F. Li, J. Gong, Y. He, and Z. Chen, Penta-MS_2 (M = Mn, Ni, Cu/Ag and Zn/Cd) monolayers with negative Poisson's ratios and tunable bandgaps as water-splitting photocatalysts, J. Mater. Chem. A **9**, 6993 (2021).

[84] H. Shu, M. Zhao, and M. Sun, Theoretical study of GaN/BP van der Waals nanocomposites with strain-enhanced electronic and optical properties for optoelectronic applications, ACS Appl. Nano Mater. **2**, 6482 (2019).

[85] C. F. Fu, J. Sun, Q. Luo, X. Li, W. Hu, and J. Yang, Intrinsic electric fields in two-dimensional materials boost the solar-to-hydrogen efficiency for photocatalytic water splitting, Nano Lett. **18**, 6312 (2018).

[86] X. Wang, Y. Li, L. Huang, X.-W. Jiang, L. Jiang, H. Dong, Z. Wei, J. Li, and W. Hu, Short-wave near-infrared linear dichroism of two-dimensional germanium selenide, J. Am. Chem. Soc. **139**, 14976 (2017).

[87] L.-S. Lu, G.-H. Chen, H.-Y. Cheng, C.-P. Chuu, K.-C. Lu, C.-H. Chen, M.-Y. Lu, T.-H. Chuang, D.-H. Wei, W.-C. Chueh *et al.*, Layer-dependent and in-plane anisotropic properties of low-temperature synthesized few-layer $PdSe_2$ single crystals, ACS Nano **14**, 4963 (2020).

[88] H. Lang, S. Zhang, and Z. Liu, Mobility anisotropy of two-dimensional semiconductors, Phys. Rev. B **94**, 235306 (2016).

[89] R. Peng, Y. Ma, B. Huang, and Y. Dai, Two-dimensional Janus PtSSe for photocatalytic water splitting under the visible or infrared light, J. Mater. Chem. A **7**, 603 (2019).

[90] B. Lu, X. Zheng, and Z. Li, Few-layer P_4O_2: A promising photocatalyst for water splitting, ACS Appl. Mater. Interfaces **11**, 10163 (2019).

[91] G. Hautier, A. Miglio, D. Waroquiers, G.-M. Rignanese, and X. Gonze, How does chemistry influence electron effective mass in oxides? A high-throughput computational analysis, Chem. Mater. **26**, 5447 (2014).

[92] E. Cadelano, P. L. Palla, S. Giordano, and L. Colombo, Elastic properties of hydrogenated graphene, Phys. Rev. B **82**, 235414 (2010).

[93] T. Lorenz, D. Teich, J.-O. Joswig, and G. Seifert, Theoretical study of the mechanical behavior of individual TiS_2 and MoS_2 nanotubes, J. Phys. Chem. C **116**, 11714 (2012).

[94] J. Yang, A. Wang, S. Zhang, J. Liu, Z. Zhong, and L. Chen, Coexistence of piezoelectricity and magnetism in two-dimensional vanadium dichalcogenides, Phys. Chem. Chem. Phys. **21**, 132 (2019).

[95] J. Qiu, X. Chen, F. Zhang, B. Zhu, H. Guo, X. Liu, J. Yu, and J. Bao, Highly adjustable piezoelectric properties in two-dimensional $LiAlTe_2$ by strain and stacking, Nanotechnology **33**, 055702 (2022).

[96] B. Mortazavi, M. Shahrokhi, B. Javvaji, A. V. Shapeev, and X. Zhuang, Highly anisotropic mechanical and optical properties of 2D $NbOX_2$ (X = Cl, Br, I) revealed by first-principle, Nanotechnology **33**, 275701 (2022).